Journal of Materials Chemistry A

ROYAL SOCIETY OF CHEMISTRY

PAPER

View Article Online
View Journal | View Issue

Check for updates

Cite this: J. Mater. Chem. A, 2025, 13, 39960

Singlet diradicaloids as n-type passivating interlayers for $CsPbI_3$ perovskite solar cells

Francesca Russo,[ab] Sofia Masi,[c] Vincenzo Tedeschi,[a] Luca Gregori,[d] Gennaro Ventruti,[e] Edoardo Mosconi,[fg] Filippo De Angelis,[d] Jhonatan Rodriguez-Pereira,[hi] Gianluca M. Farinola,[a] Francesco Fracassi,[a] Davide Blasi,*[a] Iván Mora-Seró,*[c] Andrea Listorti*[a] and Silvia Colella[j]

Received 4th June 2025
Accepted 6th October 2025

DOI: 10.1039/d5ta04509f

rsc.li/materials-a

The interface modification of halide perovskite materials is a fundamental step to obtain efficient charge extraction, passivation of defects and improved stability of polycrystalline active layers at the core of perovskite-based solar cells. For $CsPbI_3$ inorganic perovskite, this is particularly critical due to the usual formation of surface defects during perovskite crystallization, leading to increased nonradiative recombination and energy mismatch with organic transporting layers. Here we propose the use of a polychlorinated thiele hydrocarbon (TTH), *i.e.* a stable singlet diradicaloid belonging to the family of *para*-quinodimethanes, that uniquely combines the dynamic generation of a charge transfer zwitterionic excited state with excellent photostability. We proved that the use of the TTH molecule as a $CsPbI_3$ interface modifier in inverted photovoltaic devices significantly enhances the open circuit voltage of the device. This is due to a convenient synergy between efficient Pb passivation from the chlorine substituents, optimal energy level alignment and the light-triggered dipole that, overall, reduces the resistance to the charge transfer. This work paves the way to the employment of singlet diradicaloids in perovskite solar cells.

Open Access Article. Published on 14 October 2025. Downloaded on 5/4/2026 1:26:15 AM.
This article is licensed under a Creative Commons Attribution-NonCommercial 3.0 Unported Licence.

Introduction

Cesium lead triiodide ($CsPbI_3$) perovskite has garnered significant attention as a promising alternative to its organic–inorganic halide counterparts, based on MA and FA cations, in perovskite-based solar cells (PSCs). Its appeal lies in its nonvolatile nature, thermal stability and photoelectric properties. With a relatively wide bandgap of 1.60–1.72 eV, all inorganic perovskites are particularly well-suited for indoor application[1] and as sub-cells in both perovskite–silicon and perovskite tandem solar cells (PSCs).[2,3] Tandem configurations hold substantial potential for exceeding the Shockley–Queisser limit of single-junction solar cells, thereby achieving higher power conversion efficiencies (PCEs), which is a critical aspect for advancing solar technology.[4] Currently, most of the photovoltaic devices based on $CsPbI_3$ are fabricated using n–i–p architecture.[5–10] However, this architecture has certain limitations such as the use of thermophobic hole transport layers (HTLs) and high processing temperatures of electron transporting layers (ETLs), which limit their implementation in tandem solar cells.[11] In contrast, the inverted (p–i–n) structure offers several key advantages over the n–i–p design. For instance, it improves stability against air and humidity, due to its dopant-free and hydrophobic rear layer and low temperature processing, which facilitates tandem integration as a sub-cell.[12]

Nevertheless, the implementation of $CsPbI_3$ perovskite in inverted architecture poses significant additional challenges, with respect to more conventional MA/FA-based compositions. Among them, the energy level mismatch between inorganic perovskites and organic layers hampers charge extraction, leading to lower PCE and greater open-circuit voltage (V_{oc}) losses.[7,13,14]

[a]Dipartimento di Chimica, Università degli Studi di Bari "Aldo Moro", 70126 Bari, Italy. E-mail: davide.blasi@uniba.it; andrea.listorti@uniba.it
[b]Dipartimento di Ingegneria Elettrica e dell'Informazione, Politecnico di Bari, 70126 Bari, Italy
[c]Universitat Jaume I, Institute of Advanced Materials (INAM), 12071 Castelló de la Plana, Spain. E-mail: sero@uji.es
[d]University of Perugia, Department of Chemistry, Biology and Biotechnology, Via Elce diSotto 8, 06123, Perugia, Italy
[e]Dipartimento di Scienze della Terra e Geoambientali, Università di Bari, via Orabona, 4, 70125, Bari, Italy
[f]Computational Laboratory for Hybrid/Organic Photovoltaics (CLHYO) Istituto CNR di Scienze e Tecnologie Chimiche "Giulio Natta" (CNR- SCITEC), 06123 Perugia, Italy
[g]Chemistry Department, College of Science, King Saud University, 11451 Riyadh, Kingdom of Saudi Arabia
[h]Center of Materials and Nanotechnologies, Faculty of Chemical Technology, University of Pardubice, Nam. Cs. Legii 565, 53002 Pardubice, Czech Republic
[i]Central European Institute of Technology, Brno University of Technology, Purkynova 123, Brno, 61200, Czech Republic
[j]CNR NANOTEC – Istituto di Nanotecnologia – c/o Dipartimento di Chimica, Università degli Studi di Bari "Aldo Moro", 70126 Bari, Italy

This journal is © The Royal Society of Chemistry 2025

Open Access Article. Published on 14 October 2025. Downloaded on 5/4/2026 1:26:15 AM. This article is licensed under a Creative Commons Attribution-NonCommercial 3.0 Unported Licence.

During film processing, the top-surface region is prone to defect formation such as lead vacancies (V_{Pb}) and iodine–lead inversion (I_{Pb}) traps form, pinning the Fermi energy (E_f) near the valence band edge (VB). This results in inefficient electron transfer and increased nonradiative recombination at the $CsPbI_3$/fullerene interface.[15,16]

Previous studies have highlighted various promising passivating species as interlayers between the perovskite layer and the charge transporting material on top, including organic molecules,[17–19] quantum dots[20,21] and organic halide ammonium salts.[6,22] Among them, free-radical molecules have been proposed as additives for perovskites primarily serving as n-type dopants[23,24] and acting as antioxidants.[25] Recently, donor–acceptor trityl radicals bearing carbazole or aryl amine donor groups have been employed as effective hole transporting layers (HTLs) due to their favourable charge transport properties and ability to passivate interfacial defects.[26,27] In this context, polychlorinated trityl radicals are particularly well-suited, as the high number of chlorine substituents ensures efficient electronic coupling and provides multiple binding sites with perovskites. However, the presence of electron-donating groups limits the application of these derivatives as electron transporting layer (ETL) materials. Simple trityl radicals, such as tris(2,4,6-trichlorophenyl)methyl radical (TTM, shown in Fig. 1), exhibit suitable redox potentials for use as interlayers between the perovskite and the ETL.[28] Unfortunately, the lack of charge-transfer stabilization in the excited state makes these radicals highly photosensitive, limiting their use in photovoltaic devices. To address this issue, we propose the use of a polyhalogenated thiele hydrocarbon, specifically the TTM-like thiele hydrocarbon (TTH, shown in Fig. 1),[29] as an interlayer in the heterojunction between $CsPbI_3$ perovskite and C_{60}. TTH represents, to date, a rare and promising example of a photostable diradicaloid compatible with the electronic requirements of $CsPbI_3$-based devices. It shares nearly identical redox properties with the TTM radical, and its highest occupied molecular orbital (HOMO) and lowest unoccupied molecular orbital (LUMO) levels align closely with those of PCBM. However, unlike TTM, TTH offers exceptional photostability due to its singlet species nature.

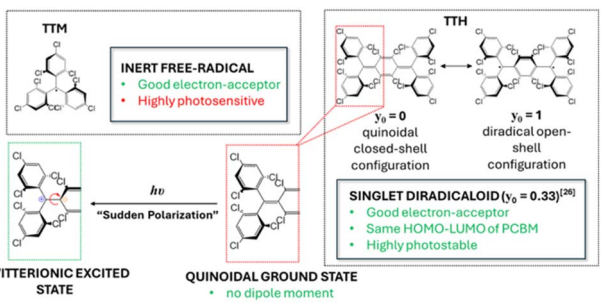

Fig. 1 Excited-state polarization. Molecular structure of the TTM radical and TTH diradicaloid and pictorial representation of the sudden polarization in the TTH excited state, where the elongation and twisting of exocyclic double bonds induces a symmetry breaking of the molecule with the consequent formation of a charge separated state (zwitterion).

TTH is the simplest TTM-based diradical and belongs to the family of singlet diradicaloids, singlet species characterized by a moderate degree of diradical character, described using the diradical index y_0, which ranges from zero (closed-shell species) to one (pure diradical), see Fig. 1.[30] In the case of TTH the y_0 exhibits a value of 0.33.

TTM-based diradicals exhibit new low-lying excited states, which are absent in TTM monoradicals, since they are ascribable to the charge resonance between the two radical subunits constituting the derivative. The excited state at higher energy is responsible for light absorption, while the lowest excited state is characterized by a double excitation and is formally dark for symmetric diradicals[31] Interestingly, in polyhalogenated thiele hydrocarbons, the two excited states can mix leading to the formation of a zwitterionic charge transfer excited state, breaking the symmetry of the molecule, driven by a sudden polarization process (the elongation and twisting of exocyclic double bonds induce the formation of a charge-separated state), as schematically shown in Fig. 1.[29,32] Therefore, despite TTH not being a zwitterion in its ground state, since it is a centrosymmetric, non-polar hydrocarbon bearing only chlorine substituents, it possesses a low-lying zwitterionic excited state, as illustrated in Fig. 1. This state emerges from the diradical character of the molecule.

While singlet diradicaloids have been proposed as emitting species in electroluminescence devices,[31,33–35] their potential application in perovskite solar cells (PSCs) remains unexplored. We applied the TTH molecule as a $CsPbI_3$ passivating layer in inverted solar cells and we found a significant increase in open circuit voltage with respect to the use of PCMB. Through a combination of theoretical modelling and experiments, we found the existence of a strong interaction between the diradicaloid molecule and the perovskite, efficiently stabilizing the $CsPbI_3$ surface in the device. Furthermore, an efficient energy alignment with respect to the perovskite energy levels enhances the electron extraction contributing to enhancing the V_{oc} of the solar cell. The zwitterionic nature of the TTH excited state could also play a role in generating an interfacial internal dipole moment that enhances the material polarization and influences the electric field within the cell, reducing the likelihood of recombination and resistances.[14,36,37] These light-triggered properties of TTH play a pivotal role in enhancing charge dynamics within the device, thereby enhancing the V_{oc}.

Results and discussion

We examined the impact of the TTH deposition layer on the device characteristics using a p–i–n cell stack: glass/indium tin oxide (ITO)/PEDOT:PSS/$CsPbI_3$/PCBM or TTH/C60/bathocuproine (BCP)/silver (Ag), where TTH and PCBM (as reference) were used as interlayers, at an optimal concentration of 0.75 mg mL^{-1} and 10 mg mL^{-1} in CB,[18] respectively (SI Fig. 3). $CsPbI_3$ has been synthesized starting from a 0.6 M solution of salts dissolved in DMF and crystallized at 210 °C for 1 min, as detailed in Methods and in SI Fig. S2 and S3 compatible with the p–i–n architecture.

Open Access Article. Published on 14 October 2025. Downloaded on 5/4/2026 1:26:15 AM.
This article is licensed under a Creative Commons Attribution-NonCommercial 3.0 Unported Licence.

Fig. 2 compares the PSCs based on the pristine cell stack (PCBM) with those embedding TTH. The statistical photovoltaic parameters from 40 devices and the *J–V* curves of the champion device are presented in Fig. 3b and c.[40] The solar cells characterization was always performed at a relative humidity below 50% and a temperature below 25 °C, to avoid fluctuation of the parameters. It is clear how the introduction of the TTH layer remarkably increased the V_{oc} from 0.69 V to 0.86 V, despite being overall limited by the PEDOT:PSS as the HTL, together with an increase in all other parameters. The film thickness of approximately 190 nm, revealed by the cross-sectional scanning electron microscopy (SEM) image of the device stack (SI Fig. S4a and b), a direct consequence of the poor solubility of CsI in polar aprotic solvents,[38,39] also strongly limits the extracted current and the overall performances.

The steady power output for this champion device sustains at 13.37 mA cm^{-2}, measuring at a fixed voltage of 0.86 V close to the maximum power point (Fig. 2).

To further verify the photocurrent enhancement, incident photon to current efficiency (IPCE) spectra were recorded (Fig. 2e) revealing the well-matched current density to the J_{sc} from *J–V* curves with an integrated current density of 13.31 and 14.14 mA cm^{-2} for the PCBM and TTH integrated devices. Moreover, iodide PSCs feature higher absorption in the long-wavelength region.[41]

The enhanced short-wavelength absorption (500–540 nm) with TTH incorporated in the cell indicates that this interlayer plays a crucial role in absorbing photons at that wavelength, contributing to the generation of electric current, either through its direct absorption (SI Fig. S5) or by enhancing charge collection efficiency at the interface. This leads to an increase in the overall efficiency of the solar cell, highlighting the formation of the dipole moment in the excited state of the diradicaloid.

The as-prepared $CsPbI_3$ films show an absorbance onset at ~736 nm in Fig. 3a indicating a band gap of 1.68 eV. The optical energy band gap was calculated using Tauc's plot by plotting a graph between $(h\nu)$ *vs.* $(\alpha h\nu)^2$.[40] Upon incorporation of the perovskite into the device, the p-type surface with deep energy-level traps can lead to uneven band bending at the PCBM/$CsPbI_3$ interface, resulting in hindered electron transfer and significant nonradiative recombination.[12,18] The undesirable electron-transfer dynamics would limit the efficiency improvement of inverted $CsPbI_3$ PSCs with low V_{oc} and FF. TTH exhibits the same LUMO energy level as PCBM Fig. 3b.[29] The steady-state normalized PL spectra (Fig. 3c) confirm the formation of the TTH excited state even when the molecule is adsorbed on the perovskite, indicating that part of the incident radiation is directly absorbed by TTH. The excitation at 570 nm reveals the presence of two distinct emission bands that are deconvoluted as shown in Fig. S6: one corresponding to the perovskite emission (peaking at 723 nm) and the other associated with one of the TTH emissions (peaking at 680 nm). TTH emission appears blue-shifted with respect to the photoluminescence of the isolated film.[29] This shift suggests a strong interaction between TTH and the perovskite surface, leading to increased molecular rigidity. In fact, a reduced Stokes shift typically indicates minimal structural reorganization in the excited state, supporting the idea of restricted molecular motion due to surface binding. This evidence points to a scenario where TTH

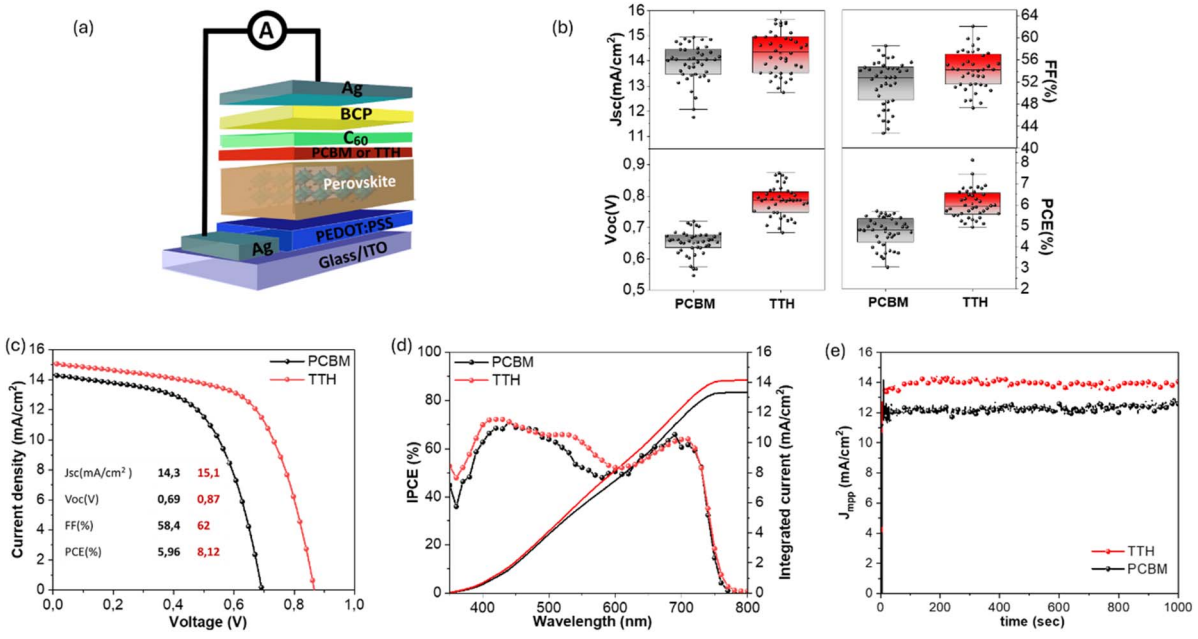

Fig. 2 Device characteristics. (a) Schematics of perovskite solar cell architecture. (b) Statistical photovoltaic parameters obtained from 40 devices for PCBM and TTH. (c) *J–V* curves of the sample PCBM (reference) and TTH p–i–n PSCs under 1-sun (100 mW cm^{-2}) illumination. (d) Maximum power point for PCBM- and TTH-embedding devices. (e) Comparison of the IPCE spectra with an integrated J_{sc} of 13.31 mA cm^{-2} and 14.13 mA cm^{-2} for PCBM and TTH, respectively. The stabilized power output under maximum power point (MPP) conditions of TTH and PCBM.

 This journal is © The Royal Society of Chemistry 2025

Open Access Article. Published on 14 October 2025. Downloaded on 5/4/2026 1:26:15 AM.
This article is licensed under a Creative Commons Attribution-NonCommercial 3.0 Unported Licence.

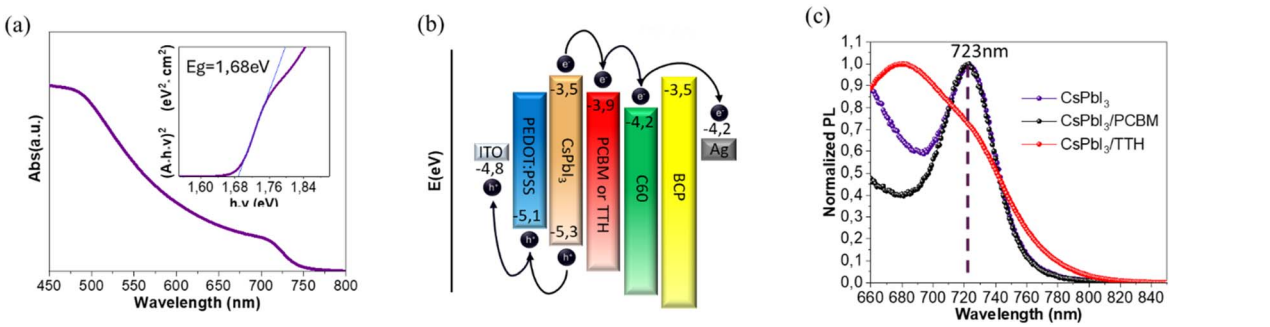

Fig. 3 Optoelectronic properties. (a) UV-VIS absorption spectra of the perovskite film and Tauc's plot to determine the energy gap of $CsPbI_3$ thin films. (b) Energy level diagram for the device. (c) Steady-state normalized PL spectra of ITO/PEDOT:PSS/$CsPbI_3$ and ITO/PEDOT:PSS/$CsPbI_3$/PCBM or TTH respectively.

is not merely passively located at the interface but actively participates in electronic processes. In this context, the observed fluorescence from TTH confirms that part of the incident radiation is absorbed by the molecule, triggering TTH excited states and as a consequence its zwitterionic nature when included as an interlayer in the perovskite device. A transient dipole formed at the interface with perovskite under working conditions.

To elucidate the electronic and optical properties of the investigated device, density functional theory (DFT) simulations were carried out, with particular emphasis on the perovskite/electron transport layer (ETL) interface. Both TTH and PCBM were considered representative ETLs.

Following the approach established in our previous studies on $MAPbI_3$ (ref. 43) and $FAPbI_3$,[44] a $CsPbI_3$ slab model was adopted, featuring a Pb-terminated surface, which is recognized as the most reactive and defect-prone termination due to the presence of undercoordinated lead atoms[45] (for further details, see Computational methods in the SI).

A complete monolayer of either TTH or PCBM molecules was subsequently adsorbed onto the $CsPbI_3$ surface. As illustrated in Fig. 4a and b, the computed adsorption energies per molecule (ΔE_{ads}) for both ETLs are negative, indicative of a thermodynamically favorable interaction with the perovskite surface and suggestive of an intrinsic protective effect.

Interestingly, PCBM displays a more pronounced interaction strength (−1.81 eV per molecule) compared to TTH (−0.84 eV per molecule), although their adsorption configurations differ substantially. PCBM coordinates the undercoordinated Pb centers *via* the carbonyl oxygen of its ester functionality, whereas TTH interacts through its chlorine atoms. This coordination modality is known to effectively mitigate trap states associated with undercoordinated lead sites.[44] Due to the steric bulk of PCBM, at equivalent molecular coverages, TTH is capable of passivating approximately twice the number of undercoordinated Pb atoms, resulting in more efficient surface passivation. This observation aligns with the experimentally observed reduction in nonradiative recombination and the corresponding increase in the open-circuit voltage (V_{oc}).

The surface passivation was verified by X-ray Photoelectron Spectroscopy (XPS) on $CsPbI_3$, $CsPbI_3$ + PCBM and $CsPbI_3$ + TTH, and the results are reported in Fig. S7 and S8 and SI Table S1. In the survey spectra in Fig. S7, C, O, I, Cs and Pb signals were detected, while Cl was identified in $CsPbI_3$ + TTH with a high resolution spectrum.

In Fig. S8, I 3d HR spectra show its characteristic spin–orbit splitting with I $3d_{5/2}$ and I $3d_{3/2}$ located at ∼618.5 and 630.0 eV, corresponding to I^- species, composing the Pb–I bonds.[46] Cs 3d HR spectra display the Cs $3d_{5/2}$ and Cs $3d_{3/2}$ doublet at ∼724.4 and 738.4 eV, which is related to the presence of Cs^+ in the 3D perovskite structure.[46] The Pb 4f HR spectra exhibit the characteristic spin–orbit splitting of Pb $4f_{7/2}$ and Pb $4f_{5/2}$ positioned at ∼137.6 and 142.5 eV, assigned to Pb^{2+} incorporated within $[PbX_6]^{4-}$ octahedral units.[46] The Cl 2p HR spectrum of the TTH sample shows its characteristic spin–orbit splitting of Cl $2p_{3/2}$ and Cl $2p_{1/2}$ at 200.3 and 201.9 eV, which revealed the presence of organic Cl (C–Cl) from TTH.[47] A chemical shifting in the main signals of the perovskite towards higher binding energy (BE) when PCBM is added to the $CsPbI_3$ perovskite was observed (values of the shifting: Cs 3d (0.4 eV), Pb 4f (0.5 eV) and I 3d (0.7 eV)), while when TTH is added the shifting occurs in the opposite direction, towards lower BE (values of the shifting: Cs 3d (0.4 eV), Pb 4f (0.4 eV) and I 3d (0.3 eV)). The different chemical surroundings leading to different binding energies are likely responsible for the better passivation of TTH. This suggests a different nature of the interface between CsPbI3 and the different molecules. In particular, as we can see in Table SI2, the contribution to the adsorption energy for TTH is totally associated with the dispersion interaction (D3) while PCBM also shows a covalent component. Moreover, to further investigate the nature of the perovskite/ETL interaction and to quantify the extent of charge transfer across the perovskite interface, we have resorted to a charge displacement (CD) analysis,[48] which allows us to visualize the displacement of charge occurring from the non-interacting perovskite and ETL fragments to the interacting heterointerface. We performed the CD analysis on the half coverage interface to evaluate the effect of one molecule. As we can see in Fig. 4c and d, the amount of charge accumulation at the interface between perovskite and PCBM is larger than that in the TTH case in line with the highest adsorption energy and the presence of covalent contribution. This different electronic

Open Access Article. Published on 14 October 2025. Downloaded on 5/4/2026 1:26:15 AM.
This article is licensed under a Creative Commons Attribution-NonCommercial 3.0 Unported Licence.

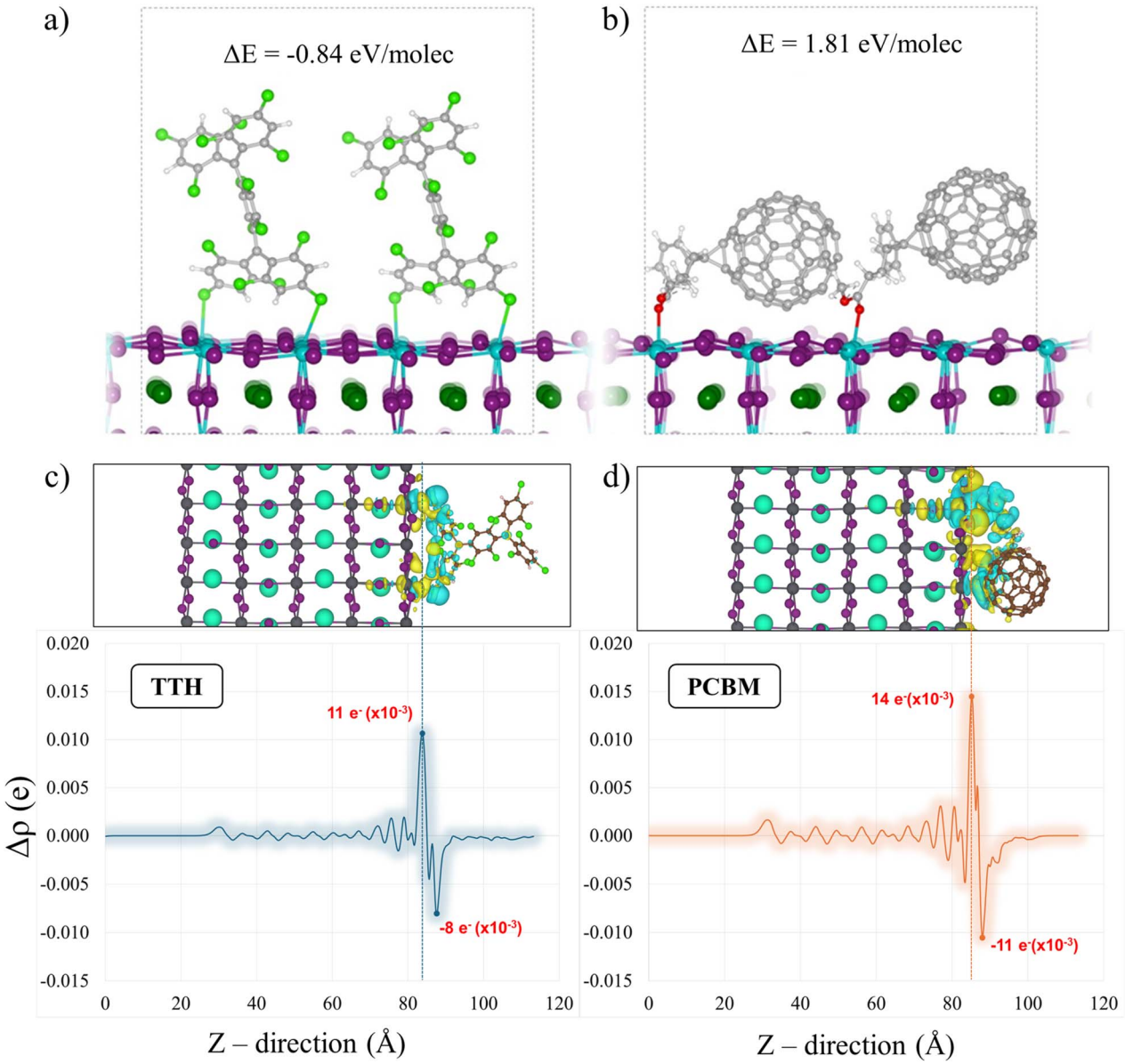

Fig. 4 Optimized geometry of the perovskite/ETL interface with (a) TTH and (b) PCBM. The ΔE_{ads} in eV is also reported. The real space plot of the charge redistribution upon adsorption and the planar-average profile along the z-axis for the (c) TTH and (d) PCBM molecules. In the real space plots, the isosurface level was set to 0.002 e Å^{-3}; the blue isosurface indicates charge depletion and the yellow isosurface indicates charge accumulation. In the profile diagrams, the perovskite slab boundaries are indicated by blue dotted lines.

character could be related to the different XPS behavior found experimentally.

Besides the passivation of the surface, the intrinsic dipole moment of the TTH molecule in its excited state may further contribute to the V_{oc} enhancement. Unfortunately, we are not able, at this stage, to reproduce this kind of excited state in our model considering the large interface model under periodic boundary conditions. We previously reported this effect on a different molecule, demonstrating the possibility of the VB and CB level tuning of the perovskite under the effect of the adsorbed species dipole.[37] Considering the formation of the TTH dipole under illumination at the perovskite interface as proved by PL, we can confidently assume the presence of such an effect also in our system.

To further investigate the role of TTH, impedance spectroscopy (IS) was conducted under open-circuit conditions with different light intensities for TTH and PCBM based solar cells.[49] The Nyquist plots at V_{oc} of impedance spectra at 1 sun are presented in Fig. 5a. As it is generally observed in PSCs, we detected principally two different semicircles, in low-frequency (LF) and high-frequency (HF) ranges. In the devices measured a decrease in the width of the arc is observed when TTH is used which indicates a lower resistance or better transport due to the presence of TTH at the interface with perovskite which will result in higher PCE. These data were modeled with an

 This journal is © The Royal Society of Chemistry 2025

Open Access Article. Published on 14 October 2025. Downloaded on 5/4/2026 1:26:15 AM.
This article is licensed under a Creative Commons Attribution-NonCommercial 3.0 Unported Licence.

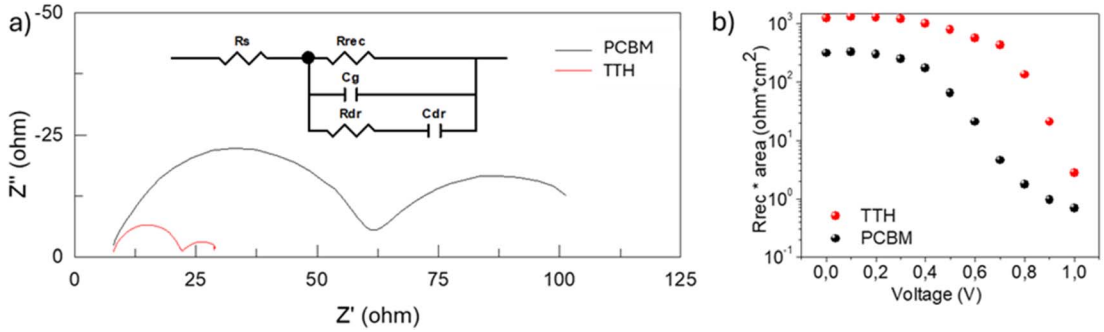

Fig. 5 Electrical characterization. (a) Nyquist plots at open-circuit voltage under 1 sun illumination intensity; inset: an equivalent circuit model composed of a series resistance, R_s, and recombination resistance, R_{rec}, obtained as the sum of HF and LF arcs, considering the transport resistance negligible, which is in parallel to a HF capacitance, C_g, the geometrical capacitance, and an RC branch (C_{dr} and R_{dr}), that splits the pattern into HF and LF arcs;[42] (b) plot of recombination resistance (R_{rec}) *versus* applied voltage of devices based on PCBM and TTH as ETMs.

equivalent circuit previously reported as shown in the inset of Fig. 5a.[42] In particular, the recombination resistance, R_{rec}, see Fig. 5b, has been obtained by the fitting of impedance measurements, as the sum of the resistances of HF and LF arcs, considering transport resistance to be negligible.[42] In the presence of the TTH layer the recombination resistance increases, which in turn implies a decrease in the nonradiative recombination rate. The recombination losses are effectively reduced by TTH, in line with the observed increase in the V_{oc}. This could be due to the improved interface matching which induces halide perovskite passivation, as confirmed by DFT, reduction of interfacial recombination and the formation of the dipole at the excited state. The lower surface recombination also contributes to the enhancement of photocurrent[50] as observed in Fig. 3.

Conclusions

We have effectively implemented a singlet diradicaloid, namely the TTM-like thiele hydrocarbon (TTH), as an interface modifier of $CsPbI_3$ perovskite in substitution of the typically used PCBM, for passivating the p-type surface with deep energy-level traps that leads to uneven band bending at the ETL/$CsPbI_3$ interface, resulting in hindered electron transfer and significant non-radiative recombination. This class of molecules, used for the first time in perovskite solar cells, offers exceptional photostability and polarization upon illumination, at the molecular level. By XPS we verified the presence of a significant interaction between TTH and the perovskite surface that was found to be very favorable by DFT. TTH interacts with the undercoordinated Pb through the chlorine atoms, providing overall a more efficient passivation of the surface with respect to PCBM. Photoluminescence and IPCE further indicate that the molecule is not just passively present at the interface but is actively involved in electronic processes. Upon 1 sun illumination, TTH is directly promoted to an excited state, suggesting that its photoexcitation contributes to the interfacial charge dynamics. Impedance spectroscopy revealed an increase in recombination resistance, which implies a decrease in the nonradiative recombination rate. The recombination losses are effectively reduced by TTH, resulting in an increase of the V_{oc} in the solar cell.

The relative PCE enhancements observed upon TTH incorporation provide a clear validation of its functional role in modulating interfacial energetics and suppressing nonradiative recombination. These improvements are fully consistent with the spectroscopic, electrochemical, and theoretical evidence presented, which collectively confirm the effectiveness of TTH in defect passivation and interface dipole formation. More broadly, this work demonstrates how the rational design of molecular interface modifiers with tailored photophysical properties can directly influence interfacial charge dynamics in perovskite devices.

Beyond its application in photovoltaics, the unique combination of photostability, photoactivity, and directional charge interaction exhibited by TTH underscores the potential of this emerging class of photoresponsive diradicaloid molecules for a wider range of perovskite-based optoelectronic technologies. In particular, their integration could benefit light-emitting diodes, photodetectors, and other architectures where precise interface control is critical for performance and stability. As such, TTH represents not only a functional alternative to conventional fullerene-based materials, but also a molecular platform for the development of next-generation hybrid interfaces.

Materials and methods

Materials

Unless otherwise stated, all materials were used as received without further purification. Cesium iodide (CsI, Anhydro-Beads™, 99.999% trace metals basis (perovskite grade)) was purchased from Sigma-Aldrich. Dimethylammonium chloride (for synthesis) was purchased from Sigma-Aldrich. Poly(3,4-ethylenedioxythiophene)–poly(styrenesulfonate) (PEDOT:PSS) aqueous solution (PVP AI 4083) was purchased from Ossila and [6,6]-phenyl C_{61} butyric acid methyl ester (PCBM) and fullerene C_{60} (sublimed, 99.99%) were purchased from nano-C. Bathocuproine (BCP) sublimated grade (purity > 99.5%) was purchased from Ossila. Dimethylformamide (DMF) anhydrous

Open Access Article. Published on 14 October 2025. Downloaded on 5/4/2026 1:26:15 AM. This article is licensed under a Creative Commons Attribution-NonCommercial 3.0 Unported Licence.

99.8% and chlorobenzene (CB) anhydrous 99.8% were purchased from Sigma-Aldrich.

$DMAPbI_3$ powder synthesis

The $DMAPbI_3$ precursor was prepared by dissolving PbI_2 (4.62 g) in DMF (10 mL) and then adding HI (3.6 mL), followed by stirring at 50 °C overnight to ensure complete reaction. To remove excess HI, the precursor was then washed with absolute ethanol to obtain a light-yellow precipitate. The obtained powder was dried in a vacuum at 65 °C for 12 h and stored in a nitrogen glovebox[51,52] and characterized (SI Fig. S2a and b).

Perovskite solution

CsI and $DMAPbI_3$ powder in a molar ratio of 1 : 1 were dissolved in 1 mL DMF to obtain a final concentration of 0.6 M, followed by stirring for 1 h at 60 °C. To regulate the crystallization process of the $CsPbI_3$ perovskite films, DMACl was incorporated into the precursor solutions at a concentration of 2,28 mg mL^{-1}.[5]

TTH synthesis

TTH was synthesized according to a procedure reported in the literature.[29]

Device fabrication

Pre-patterned ITO glasses were washed with detergent solution (Semico Clean 56, Furuuchi Chemical), water, and isopropanol, followed by drying with an air gun and UV-ozone treatment was performed before the hole transport layer (HTL) deposition. The PEDOT:PSS hole transport layer was fabricated from an aqueous dispersion which was filtered through a 0.45 μm PVDF filter and then spin coated on the ITO substrate in air, using a spin program of 3500 rpm for 40 s, and annealed at 80 °C for 1 min and 120 °C for 30 min, and then cooled to room temperature. Subsequently, the glass/ITO substrates with PEDOT:PSS deposited were transferred into a nitrogen-filled glove box. Cesium lead iodide solution was spin-coated on PEDOT:PSS and processed at 3000 rpm for 30 s without dripping. The obtained films were subsequently annealed onto a hot plate at 210 °C for 1 min and then cooled to room temperature. The temperature in the glove-box needs to be kept below 24 °C in order to obtain reproducible film characteristics. PCBM (10 mg mL^{-1} in CB) and TTH (0.75 mg mL^{-1} in CB) were spin-coated at 2000 rpm for 45 seconds and dried in a N_2 glove box at room temperature without annealing for 20 minutes. The perovskite-coated samples were moved under N_2 to a vacuum deposition chamber, where 20 nm of C_{60} (deposition rate 0.01 nm s^{-1}) and 8 nm of BCP (deposition rate 0.01 nm s^{-1}) were deposited by thermal evaporation. The top electrode was prepared by depositing 110 nm of Ag through a shadow mask. The deposition rate for Ag was first set at 0.005 nm s^{-1} to reach 5 nm, then raised to 0.01 nm s^{-1} to reach 20 nm, and finally raised to 0.08 nm s^{-1} to reach the target thickness.

Characterization techniques

Photoluminescence (PL) spectra. Photoluminescence (PL) spectra were collected by using a Fluorolog®-3 spectrofluorometer (HORIBA Jobin-Yvon, Edison, NJ, USA), equipped with a 450 W xenon lamp as the excitation source and double grating excitation and emission monochromators. The PL emission spectra were recorded at ambient temperature by using an excitation wavelength of 570 nm.

Incident-photon-to current conversion efficiency (IPCE). IPCE was measured using a QEPVSI-b Oriel measurement system and measured in DC mode.

Electrochemical impedance spectroscopy (EIS) measurements. Electrochemical impedance spectroscopy (EIS) measurements were performed by applying 20 mV voltage perturbation at different frequencies from 1 MHz to 0.1 Hz on a PGSTAT-30 from Autolab and under 1 sun illumination at different applied potentials, from 0 to 1.2 volts. A Xe lamp was used to illuminate the PSC controlling the light intensity with neutral density filters, at 1 sun (100 mW cm^{-2}) on a logarithmic scale. The AC voltage perturbation was fixed at 20 mV under open-circuit conditions. The integration time was fixed at 0.125 s and the number of cycles was equal to 1. Each frequency spectrum was measured ranging between 1 MHz and 0.1 Hz. The recombination resistance was calculated by using the equivalent circuit previously reported.[42]

Solar cell characterization. The current voltage (J–V) curves are measured using a Keithley 2612 source meter under AM 1.5G (1000 W m^{-2}) provided using a solar simulator from Abet and xenon short-arc lamp Ushio 150 watts, in the air at a temperature of around 25 °C and without encapsulation. Each curve is generated using 123 data points from a starting potential of 1.2 V to a final potential of −0.02 V (reverse scan; *vice versa* for the forward scan) using a scan rate of 10 mV s^{-1}. The active area of the cell is 0.121 cm^2. The operation stability was evaluated by maximum power point tracking under continuous 1 sun illumination.

X-ray diffraction. XRD patterns for structural investigations were collected using a PANalytical Empyrean diffractometer equipped with a 1.8 kW CuKα ceramic X-ray tube ($\lambda = 1.5418$ Å) and a real time multiple strip (RTMS) PIXcel3D detector. Analytical conditions were 40 mA and 40 kV, a scanning speed of 0.026° s^{-1}, and a 2θ range from 7° to 80°. To minimize background noise coming from the holder and to improve the signal to background in a powder pattern, a zero-background holder (ZBH) made of a single crystal silicon cut at a special orientation parallel to the Si (510) plane was used. All powdered samples were packed in a shallow cavity of 8 mm diameter and 0.2 mm thickness and all measurements were performed at room temperature.

Attenuated total reflectance – Fourier transform infrared spectroscopy (ATR-FTIR). A vacuum Bruker Vertex 70v Fourier transform infrared spectrometer was used to record the infrared absorption spectra of perovskite thin films deposited on glass in the range 400–4000 cm^{-1} over 32 scans with a resolution of 4 cm^{-1}. Spectra were collected in attenuated total reflectance

 This journal is © The Royal Society of Chemistry 2025

Open Access Article. Published on 14 October 2025. Downloaded on 5/4/2026 1:26:15 AM. This article is licensed under a Creative Commons Attribution-NonCommercial 3.0 Unported Licence.

mode utilizing an ATR module equipped with a single reflection diamond ATR crystal (refractive index of 2.4).

Scanning electron microscopy (SEM). The topographical and cross-sectional images were recorded using a field emission scanning electron microscope (FEG-SEM) JEOL 3100F operated at 5 kV. The SEM was recorded from films deposited on top of the ITO substrate.

X-ray photoelectron spectroscopy (XPS). The surface chemistry, composition, and electronic state were determined by X-ray Photoelectron Spectroscopy (XPS, ESCA-2SR, Scienta-Omicron). The spectra were recorded at a pass energy of 150 eV for survey and 30 eV for high-resolution (HR), respectively, by employing monochromatic Al Kα = 1486.6 eV, operated at 200 W and 12.5 kV. The surface charge was compensated for by using a charge neutralizer (CN-10) operated at 7 μA and 1 eV. Adventitious carbon (284.8 eV) was utilized for reference on the binding energy scale. CasaXPS processing software (Casa Software Ltd) was used to analyze the data.

Computational details

The calculations were based on the experimental crystal structure of $CsPbI_3$ obtained from the work of Sutton *et al.*[53] We fixed the lattice parameters to the orthorhombic black phase with a = 8.856 Å, b = 8.577 Å and c = 12.472 Å and relaxed only the ions inside the unit cell. All calculations were performed using the Quantum Espresso packages,[54,55] employing density functional theory (DFT) at the PBE level of theory within the generalized gradient approximation (GGA). To account for van der Waals interactions, the Perdew–Burke–Ernzerhof (PBE) functional was employed with DFT-D3 dispersion corrections.[56] Norm conserving pseudopotential from the dojo04 repository[57] was used to describe core-valence interactions, with a kinetic energy cutoff of 60 Ry for the wavefunction and 240 Ry for the charge density. A gamma-centered k-point grid of 4 × 4 × 2 was employed for Brillouin zone sampling of the unit cell. To refine the electronic structure predictions and improve the accuracy of band gap estimations, the hybrid exchange–correlation functional HSE06 (ref. 58) was utilized, with the exact exchange parameter set to 0.43. The calculated band gap at the PBE level of theory is 1.67 eV, and with HSE06-SOC it is 1.71 eV, which agrees well with the experimental band gap of 1.69 obtained from this work.

Once the unit cell was fully analyzed, we extended our study to the surfaces. A 2 × 2 in-plane supercell was constructed, and the perpendicular direction was cleaved to create the (001) surface by adding a 20 Å of vacuum. Two distinct terminations were investigated: the CsI-terminated surface, referred to as "passivated," and the PbI_2-terminated surface, referred to as "unpassivated". Hence, we focused only on the PbI_2 terminated surface and we studied the difference in adsorption and the consequential changes in the electronic properties of the perovskite materials by adsorbing the PCBM and TTH molecules as ETL materials. The adsorption energy (E_{ads}) is calculated following this equation:

$$\Delta E_{ads} = [E_{molecule\text{-}slab} - (E_{pristine} - n \times E_{molecule})]/n \quad (1)$$

where $E_{molecule\text{-}slab}$ is the total energy of the passivated slab; $E_{pristine}$ is the total energy of the pristine PbI_2- or MAI-terminated bare surface and molecule is the energy of the isolated molecule. We normalize E_{ads} by dividing by the number of molecules (n) corresponding to the number of the molecules adsorbed on the surfaces. Finally, the energy positions of the valence band maxima (VBM) on differently terminated surfaces were quantified by calculating the associated ionization energy (IE). The IE is defined here as the energy required to extract electrons from the valence band and is distinguished from the work function of the slab, which is the energy required to extract electrons from the Fermi level and is significantly influenced by carrier densities and surface defects.

IEs were calculated by using the expression:

$$IE = E_{vac} - E_{VBM} \quad (2)$$

The bulk $CsPbI_3$ VBMs used in eqn (2) were obtained by matching the electrostatic potential in the slab to that in bulk $CsPbI_3$. In eqn (2) E_{vac} is the potential in the vacuum, *i.e.* the sum of the pseudo and Hartree potentials (V_{PS} + V_H) in the vacuum region between periodic slabs, and E_{VBM} is the energy of the top of the valence band of bulk $CsPbI_3$.

Author contributions

FR, AL and SC conceived the experiments and wrote the draft, FR fabricated the solar cells, DB and GMF designed the molecule, VT and DB developed the synthesis, EM, FDA, and LG conceived and ran the simulations, SM and IMS conceived and ran the EIS experiments, GV performed the structural characterization, AL and FF performed the optical characterization, JRP performed the XPS measurements and analysis, SC coordinated the work, and all the authors discussed the results and worked on the manuscript.

Conflicts of interest

There are no conflicts to declare.

Data availability

The data supporting this article have been included as part of the supplementary information (SI). Supplementary information is available. See DOI: **https://doi.org/10.1039/d5ta04509f**.

Acknowledgements

This work was supported by the Italian Ministry of Environment and Energy Security in the framework of the Project GoPV (CSEAA_00011) for Research on the Electric System. S. C. acknowledges the PRIN 22 and PRIN PNRR 22 projects INTERFACE (2022HWWW3S) and DELPHI (P2022W9773). AL acknowledges the PRIN2022 project REVOLUTION, CUP:2022HRZH7P. E. M. acknowledges PRIN2022PNRR BEAGLE, CUP: P20223HSWX. E. M. acknowledges financial support under the National Recovery and Resilience Plan

Open Access Article. Published on 14 October 2025. Downloaded on 5/4/2026 1:26:15 AM. This article is licensed under a Creative Commons Attribution-NonCommercial 3.0 Unported Licence.

(NRRP), Mission 4, Component 2, Investment 1.1, Call for tender No. 104 published on 2.2.2022 by the Italian Ministry of University and Research (MUR), funded by the European Unisia – NextGenerationEU – Project Title 2022HRZH7P – Re-evolutionary solar fuel production envisioning water stable lead-free perovskite exploitation – REVOLUTION – CUP B53D23015350006 – Grant Assignment Decree No. 1064 adopted on 18.7.2022 by the Italian Ministry of University and Research (MUR). V. T. acknowledges financial support under the National Recovery and Resilience Plan (NRRP), D. M. 117/2023, Investment 3.3, CUP: H91I23000230007. The authors acknowledge the Ministry of Education, Youth and Sports of the Czech Republic, for the financial support of XPS measurements using the CEMNAT infrastructure (project LM 2023037). This work was supported by the Ministry of Science and Innovation of Spain under the projects ConFlex (PID2023-151880OB-C33). S. M. acknowledges financial support from UJI with the project UJI-2023-01.

Notes and references

1 K.-L. Wang, H. Lu, M. Li, C.-H. Chen, D.-B. Zhang, J. Chen, J.-J. Wu, Y.-H. Zhou, X.-Q. Wang, Z.-H. Su, Y.-R. Shi, Q.-S. Tian, Y.-X. Ni, X.-Y. Gao, S. M. Zakeeruddin, M. Grätzel, Z.-K. Wang and L.-S. Liao, *Adv. Mater.*, 2023, **35**, 2210106.

2 A. Ho-Baillie, M. Zhang, C. F. J. Lau, F.-J. Ma and S. Huang, *Joule*, 2019, **3**, 938–955.

3 H. H. Jin, F. Zhang, C. Xiao, J. H. Su, K. P. Jin, J. J. Berry, K. Zhu and S. H. Im, *Joule*, 2021, **5**, 481–494.

4 K. Wang, Y. Tong, L. Cao, S. Yue, Y. Li, C. Li, M. Wu and H. Wang, *Cell Rep. Phys. Sci.*, 2023, **4**, 101726.

5 S. Li, J. Qiu, R. Zhuang, Q. Zhou, M. Zhang, M. Yu, Y. Hua and X. Zhang, *ACS Appl. Energy Mater.*, 2023, **6**, 3514–3524.

6 L. Wu, G. Li, K. Prashanthan, A. Musiienko, J. Li, T. W. Gries, H. Zhang, H. Köbler, P. Janasik, A. N. S. Appiah, G. Paramasivam, T. Sun, M. Li, D. Marongiu, M. Saba and A. Abate, *Adv. Mater.*, 2023, **35**, 2304150.

7 S. Yang, M. Wu, X. Lei, J. Wang, Y. Han, X. He, S. Liu and Z. Liu, *ACS Energy Lett.*, 2024, **9**, 4817–4826.

8 R. Li, S. Zhang, H. Zhang, Z. Wang, X. Feng, Y. Du, T. Zhou, X. Chen, P. Liu, L. Liu, J. Zhang, Q. Chen, L. Xi, K. Zhao, F. L. Shengzhong and Q. Tian, *Angew. Chem., Int. Ed.*, 2024, **63**, e202410600.

9 Z. Wang, Q. Chen, H. Xie, X. Feng, Y. Du, T. Zhou, R. Li, J. Zhang, L. Zhang, Z. Xu, L. Xi, Q. Tian and F. L. Shengzhong, *Adv. Funct. Mater.*, 2025, **35**, 2416118.

10 Z. Wang, Q. Tian, H. Zhang, H. Xie, Y. Du, L. Liu, X. Feng, A. Najar, X. Ren and F. L. Shengzhong, *Angew. Chem., Int. Ed.*, 2023, **62**, e202305815.

11 S. Fu, J. Le, X. Guo, N. Sun, W. Zhang, W. Song and J. Fang, *Adv. Mater.*, 2022, **34**, 2205066.

12 K. Wang, Z. Su, Y. Chen, H. Qi, T. Wang, H. Wang, Y. Zhang, L. Cao, Q. Ye, F. Huang, Y. Tong and H. Wang, *J. Mater. Sci. Technol.*, 2022, **114**, 165–171.

13 T. Li, J. Xu, R. Lin, S. Teale, H. Li, Z. Liu, C. Duan, Z. Qian, K. Xiao, P. Wu, B. Chen, S. Jiang, S. Xiong, H. Luo, S. Wan, L. Li, Q. Bao, Y. Tian, X. Gao, X. Jin, E. H. Sargent and H. Tan, *Nat. Energy*, 2023, **8**, 610–620.

14 B. Li, S. Li, J. Gong, X. Wu, Z. Li, D. Gao, D. Zhao, C. Zhang, Y. Wang and Z. Zhu, *Chem*, 2024, **10**, 35–47.

15 Y. Duan, J. Wang, D. Xu, P. Ji, H. Zhou, Y. Li, S. Yang, Z. Xie, X. Hai, X. Lei, R. Sun, Z. Fan, K. Zhang, S. Liu and Z. Liu, *Adv. Funct. Mater.*, 2024, **34**, 2312638.

16 X. Gu, W. Xiang Prof., Q. Tian Prof. and S. (Frank) Liu Prof., *Angew. Chem. Int*, 2021, **60**, 23164–23170.

17 B. Yang, J. Suo, E. Mosconi, D. Ricciarelli, W. Tress, F. De Angelis, H.-S. Kim and A. Hagfeldt, *ACS Energy Lett.*, 2020, **5**, 3159–3167.

18 X. Guo, C. Lu, W. Zhang, H. Yuan, H. Yang, A. Liu, Z. Cui, L. Wen, Y. Hu, X. Li and J. Fang, *ACS Energy Lett.*, 2024, **9**, 329–335.

19 J. Qi, J. Tong, Y. Xian, R. A. Kerner, S. P. Dunfield, C. Xiao, R. A. Scheidt, D. Kuciauskas, X. Wang, M. P. Hautzinger, R. Tirawat, M. C. Beard, D. P. Fenning, J. J. Berry, B. W. Larson, Y. Yan and K. Zhu, *Nature*, 2022, **611**, 278–283.

20 K. M. Muhammed Salim, S. Masi, A. Fabián Gualdrón-Reyes, R. S. Sánchez, E. M. Barea, M. Krecmarová, J. F. Sánchez-Royo and I. Mora-Seró, *ACS Energy Lett.*, 2021, **6**, 3511–3521.

21 J. Ni, J. Guan, M. Hu, R. Wang, Z. Yang, J. Li, S. Zhang, L. Sen, J. Li, H. Cai and J. Zhang, *ACS Appl. Energy Mater.*, 2023, **6**, 11090–11099.

22 Z. Xu, N. Liu, X. Liu, W. Han, W. W. Xu, J. Zhang, L. Huang, Z. Hu and Y. Zhu, *Chem. Eng. J.*, 2023, **451**, 139047.

23 B. Tuo, Z. Wang, Z. Ren, H. Zhang, X. Lu, Y. Zhang, S. Zang and Y. Song, *Energy Environ. Sci.*, 2024, **17**, 2945–2955.

24 H. Chen, Y. Zhan, G. Xu, W. Chen, S. Wang, M. Zhang, Y. Li and Y. Li, *Adv. Funct. Mater.*, 2020, **30**, 2001788.

25 F. Bisconti, M. Leoncini, S. Gambino, N. Vanni, S. Carallo, F. Russo, V. Armenise, A. Listorti, S. Colella, S. Valastro, A. Alberti, G. Mannino and A. Rizzo, *ACS Nano*, 2024, **18**, 1573–1581.

26 M. Stanitska, R. Keruckiene, G. Sini, D. Volyniuk, A. Marsalka, Z.-E. Shi, C.-M. Liu, Y.-R. Lin, C.-P. Chen and J. V. Grazulevicius, *ACS Appl. Mater. Interfaces*, 2024, **16**, 41230–41243.

27 P. Xie, H. Xiao, Y. Qiao, G. Qu, J. Chen, X. Liu and Z. Xiang, *Chem. Eng. J.*, 2023, **462**, 142328.

28 A. Y. Tesio, D. Blasi, M. Olivares-Marín, I. Ratera, D. Tonti and J. Veciana, *Chem. Commun.*, 2015, **51**, 17623–17626.

29 A. Punzi, Y. Dai, C. N. Dibenedetto, E. Mesto, E. Schingaro, T. Ullrich, M. Striccoli, D. M. Guldi, F. Negri, G. M. Farinola and D. Blasi, *J. Am. Chem. Soc.*, 2023, **145**, 20229–20241.

30 K. Yamaguchi, *Chem. Phys. Lett.*, 1975, **33**, 2.

31 D. Mesto, M. Orza, B. Bardi Dr, A. Punzi Prof., I. Ratera Dr, J. Veciana Prof., G. Farinola Prof., A. Painelli Prof., F. Terenziani Prof., D. Blasi Dr and F. Negri Prof., *Chem. Eur. J.*, 2025, **31**, e202500749.

32 L. Cheng-Hao, Z. He, C. Ruchlin, Y. Che, K. Somers and D. F. Perepichka, *J. Am. Chem. Soc.*, 2023, **145**, 15702–15707.

33 P. Y. Craig, R. Chowdhury, Y. Fu, P. Ghosh, W. Zeng, T. B. E. Mustafa, J. Grüne, L. E. Walker, D. G. Congrave, X. W. Chua, P. Murto, A. Rao, H. Sirringhaus, F. Plasser,

 This journal is © The Royal Society of Chemistry 2025

Open Access Article. Published on 14 October 2025. Downloaded on 5/4/2026 1:26:15 AM. This article is licensed under a Creative Commons Attribution-NonCommercial 3.0 Unported Licence.

C. P. Grey, R. H. Friend and H. Bronstein, *Sci. Adv.*, 2024, **10**, eado3476.

34 Y. Zhu, Z. Zhu, S. Wang, Q. Peng Prof. Dr. and A. Abdurahman Prof. Dr., *Angew. Chem., Int. Ed.*, 2025, **64**, e202423470.

35 L. Matasovi, H. Bronstein, R. H. Friend and F. Plasser, *R. Soc. Chem. Adv.*, 2024, **254**, 107–129.

36 S. Tan, N. Zhou, Y. Chen, L. Li, G. Liu, P. Liu, C. Zhu, J. Lu, W. Sun, C. Qi and H. Zhou, *Adv. Energy Mater.*, 2019, **9**, 1803024.

37 L. Gregori, D. Meggiolaro and F. De Angelis, *ACS Energy Lett.*, 2024, **9**, 5329–5333.

38 Y. Jiang, J. Yuan, Y. Ni, J. Yang, Y. Wang, T. Jiu and J. Chen, *Joule*, 2018, **7**, 1356–1368.

39 R. E. Beal, D. J. Slotcavage, T. Leijtens, A. R. Bowring, R. A. Belisle, W. H. Nguyen, G. F. Burkhard, E. T. Hoke and M. D. McGehee, *J. Phys. Chem. Lett.*, 2016, **7**, 746–751.

40 S. Fu, W. Zhang, X. Li Jianming, W. Guan and S. J. Fang, *ACS Energy Lett.*, 2021, **6**, 10.

41 Y. Wang Dr., X. Liu, T. Zhang Dr., X. Wang, M. Kan, J. Shi and Y. Zhao Prof., *Angew. Chem.*, 2019, **131**, 16844–16849.

42 S.-M. Yoo, S. J. Yoon, J. A. Anta, H. J. Lee, P. P. Boix and I. Mora-Seró, *Joule*, 2019, **3**, 2535–2549.

43 B. Yang, J. Suo, D. Bogachuk, W. Kaiser, C. Baretzky, O. Er-Raji, G. Loukeris, A. A. Alothman, E. Mosconi, M. Kohlsta, U. Würfel, F. De Angelis and A. Hagfeldt, *Energy Environ. Sci.*, 2024, **17**, 1549.

44 J. Suo, B. Yang, E. Mosconi, D. Bogachuk, T. A. S. Doherty, K. Frohna, D. J. Kubicki, F. Fu, Y. J. Kim, O. Er-Raji, T. Zhang, L. Baldinelli, L. Wagner, A. N. Tiwari, F. Gao, A. Hinsch and S. D. Stranks, Filippo De Angelis & Anders Hagfeldt, *Nat. Energy*, 2024, **9**, 172–183.

45 D. Meggiolaro, E. Mosconi, A. H. Proppe, R. Quintero-Bermudez, S. O. Kelley, E. H. Sargent and F. De Angelis, *ACS Energy Lett.*, 2019, **4**(9), 2181–2184.

46 A. F. Gualdró-Reyes, J. Rodríguez-Pereira, E. Amado-Gonzalez, R.-P. Jorge, R. Ospina, S. Masi, S. J. Yoon, J. Tirado, F. Jaramillo, S. Agouram, V. Muñoz-Sanjose, S. Gimenez and I. Mora-Sero, *ACS Appl. Mater. Interfaces*, 2020, **12**, 914–924.

47 J. F. Moulder, W. F. Stickle, P. E. Sobol and K. D. Bomben, *Handbook of X-Ray Photoelectron Spectroscopy*, Physical Electronics, Inc., Eden Prairie, Minnesota, 1995, pp. 63–218.

48 E. Mosconi, E. Ronca and F. De Angelis, *J. Phys. Chem. Lett.*, 2014, **5**, 2619–2625.

49 D. Pitarch-Tena, T. T. Ngo, M. Vallés-Pelarda, T. Pauporte and I. Mora-Seró, *ACS Energy Lett.*, 2018, **3**, 1044.

50 J. Idígoras, L. Contreras-Bernal, J. M. Cave, N. E. Courtier, Á. Barranco, A. Borras, J. R. Sánchez-Valencia, J. A. Anta and A. B. Walker, *Adv. Mater. Interfaces*, 2018, **5**, 1801076.

51 Y. Pei, L. Yang, F. Li, S. Bai, X. Jian and M. Liu, *iScience,*, 2019, **15**, 165–172.

52 Y. Cui, J. Shi, F. Meng, B. Yu, S. Tan, S. He, C. Tan, Y. Li, H. Wu, Y. Luo, D. Li and Q. Meng, *Adv. Mater.*, 2022, **34**, 2205028.

53 R. J. Sutton, M. R. Filip, A. A. Haghighirad, N. Sakai, B. Wenger, F. Giustino and H. J. Snaith, *ACS Energy Lett.*, 2018, **3**(8), 1787–1794.

54 P. Giannozzi, S. Baroni, N. Bonini, M. Calandra, R. Car, C. Cavazzoni, D. Ceresoli, G. L. Chiarotti, M. Cococcioni and I. Dabo, *J. Phys.: Condens. Matter*, 2009, **21**, 395502.

55 P. Giannozzi, O. Andreussi, T. Brumme, O. Bunau, M. Buongiorno Nardelli, M. Calandra, R. Car, C. Cavazzoni, D. Ceresoli and M. Cococcioni, *J. Phys.: Condens. Matter*, 2017, **29**, 465901.

56 S. Grimme, J. Antony, S. Ehrlich and H. Krieg, *J. Chem. Phys.*, 2010, **132**, 154104.

57 J. vanSetten, M. Giantomassi, E. Bousquet, M. J. Verstraete, D. R. Hamann, X. Gonze and G.-M. Rignanese, *Comput. Phys. Commun.*, 2018, **226**, 39–54.

58 H. Jochen, G. E. Scuseria and M. Ernzerhof, *J. Chem. Phys.*, 2003, **118**, 8207–8215.